RESEARCH ARTICLE

Exploratory mass cytometry analysis reveals immunophenotypes of cancer treatment-related pneumonitis

Toyoshi Yanagihara[1,2,5*], Kentaro Hata[1,5], Keisuke Matsubara[3], Kazufumi Kunimura[3], Kunihiro Suzuki[1], Kazuya Tsubouchi[1], Satoshi Ikegame[1], Yoshihiro Baba[4], Yoshinori Fukui[3], Isamu Okamoto[1]

[1] Department of Respiratory Medicine, Graduate School of Medical Sciences, Kyushu University, Fukuoka, Japan

[2] Department of Respiratory Medicine, NHO Fukuoka National Hospital, Fukuoka, Japan

[3] Division of Immunogenetics, Department of Immunobiology and Neuroscience, Medical Institute of Bioregulation, Kyushu University, Fukuoka, Japan

[4] Division of Immunology and Genome Biology, Department of Molecular Genetics, Medical Institute of Bioregulation, Kyushu University, Fukuoka, Japan

[5] These authors contributed equally to this work and share the first authorship

[*] **Corresponding author:** Toyoshi Yanagihara
E-mail: toyoshi.yana@gmail.com

Abstract

Anti-cancer treatments can result in various adverse effects, including infections due to immune suppression/dysregulation and drug-induced toxicity in the lung. One of the major opportunistic infections is *Pneumocystis jirovecii* pneumonia (PCP), which can cause severe respiratory complications and high mortality rates. Cytotoxic drugs and immune-checkpoint inhibitors (ICIs) can induce interstitial lung diseases (ILDs). Nonetheless, the differentiation of these diseases can be difficult, and the pathogenic mechanisms of such diseases are not yet fully understood. To better comprehend the immunophenotypes, we conducted an exploratory mass cytometry analysis of immune cell subsets in bronchoalveolar lavage fluid from patients with PCP, cytotoxic drug-induced ILD (DI-ILD), and ICI-associated ILD (ICI-ILD) using two panels containing 64 markers. In PCP, we observed an expansion of the $CD16^+$ T cell population, with the highest $CD16^+$ T proportion in a fatal case. In ICI-ILD, we found an increase in $CD57^+$ $CD8^+$ T cells expressing immune checkpoints ($TIGIT^+$ $LAG3^+$ $TIM\text{-}3^+$ $PD\text{-}1^+$), $FCRL5^+$ B cells, and $CCR2^+$ $CCR5^+$ $CD14^+$ monocytes. These findings uncover the diverse immunophenotypes and possible pathomechanisms of cancer treatment-related pneumonitis.

Keywords

Mass cytometry, cytometry by time-of-flight (CyTOF), *Pneumocystis jirovecii* pneumonia, immune-checkpoint inhibitor, immune-related adverse event, drug-induced interstitial lung disease

Introduction

The advancements in anti-cancer therapy have revolutionized cancer management and have led to improved patient outcomes. However, these therapies can also lead to various adverse effects, including infections due to immune suppression/dysregulation and drug-induced toxicity, with the lungs being a commonly affected organ (Conte et al., 2022)(Morelli et al., 2022)(Skeoch et al., 2018). One of the major opportunistic infections in cancer patients or those receiving immunosuppressive treatment is *Pneumocystis jirovecii* pneumonia (PCP), which can cause severe respiratory complications and high mortality rates (Thomas and Limper, 2004)(Asai et al., 2022)(Apostolopoulou and Fishman, 2022). However, the precise immune reactions during PCP development and mechanisms of lung injury remain largely unknown.

While both cytotoxic drugs and immune-checkpoint inhibitors (ICIs) can induce interstitial lung diseases (ILDs), the mechanisms underlying these complications may differ between the two classes of drugs. In particular, ICI-associated ILDs are considered a type of immune-related adverse events (irAE)(Postow et al., 2018)(Ando et al., 2021). Nonetheless, the precise mechanisms that cause drug-induced ILDs are predominantly unidentified. Further, despite various diagnostic approaches, including radiology and molecular testing, there is a need for useful biomarkers to distinguish PCP, cytotoxic drug-induced (DI)-ILD, and ICI-ILD.

Mass cytometry, also known as cytometry by time-of-flight (CyTOF), is a cutting-edge technology that uses inductively coupled plasma mass spectrometry to detect metal ions tagged to antibodies that bind to specific cellular proteins, allowing for a detailed and multi-dimensional characterization of cellular composition and function (Spitzer and Nolan, 2016). This technique provides a unique advantage over traditional flow cytometry, which is limited by spectral overlap and the number of parameters that can be analyzed simultaneously. Mass cytometry has been used to study a variety of biological systems, including immune-mediated diseases, such as cancer and autoimmune conditions (Matsubara et al., 2021)(Hata et al., 2023)(Couloume et al., 2021)(Chedid et al., 2022). Through high-throughput analysis of large numbers of single cells, mass cytometry can provide a more comprehensive understanding of the cellular heterogeneity and signaling pathways involved in these diseases, allowing for the identification of potential therapeutic targets and biomarkers.

This study aims to distinguish pulmonary involvement in patients with malignancy undergoing chemotherapy and identify potential biomarkers for DI-ILD, ICI-ILD, and PCP by analyzing bronchoalveolar lavage fluid (BALF) samples with mass cytometry.

By characterizing the cellular and molecular changes in BALF from patients with these complications, we aim to improve our understanding of their pathogenesis and identify potential therapeutic targets.

Materials and Methods

Patients

In this retrospective study, patients who were newly diagnosed with PCP, DI-ILD, and ICI-ILD and had undergone BALF collection at Kyushu University Hospital from January 2017 to April 2022 were included. The retrospective study was approved by the Ethics Committee of Kyushu University Hospital (reference number 22117-00). Diagnostic criteria for PCP, DI-ILD, and ICI-ILD were in accordance with those previously described (Skeoch et al., 2018)(Asai et al., 2022)(Apostolopoulou and Fishman, 2022)(Delaunay et al., 2019). A visual representation of the experimental and analytical workflow can be found in Figure 1.

Mass cytometry

Metal-tagged antibodies were obtained from Standard Biotools or purchased in a purified form (Supplementary Table 1) and then labeled with metals using the Maxpar Antibody Labeling Kit (Standard Biotools) as instructed by the manufacturer. The cell labeling was performed as previously described (Hata et al., 2023). Upon collection, BALF samples were immediately centrifuged at 300 g for 5 minutes to pellet the cells. The resultant cell pellets were then resuspended in Cellbanker 1 cryopreservation solution (Takara, catalog #210409). This suspension was aliquoted into cryovials and gradually frozen to –80ºC and stored at –80ºC until required for experimental analysis. Cryopreserved BALF cells were thawed in PBS and then stained with Cell-ID Cisplatin-198Pt (Standard Biotools #201198, 1:2000 dilution) in PBS before being incubated with FcR blocking reagent (Myltenyi, #130-059-901) and barcoded with each metal-labeled CD45 antibody (Supplementary Table 1). After washing, CD45-labeled cells were mixed and stained with APC-conjugated FCRL5 antibodies (for panel #2), followed by staining with the antibody cocktail (Panels #1 and #2, see Supplementary Table 1). The antibody amount was determined through preliminary experiments with metal minus one. Cells were then washed, fixed with 1.6% formaldehyde, and resuspended in Cell-ID Intercalator 103Rh (Standard Biotools #201103A) in Fix and Perm buffer (Standard Biotools) at 4□ overnight. For acquisition, cells were resuspended in MaxPar Cell Acquisition Solution (Standard Biotools #201240) containing one-fifth

EQ Four Element Calibration Beads (Standard Biotools #201078) and acquired at a rate of 200-300 events/second on a Helios mass cytometer (Standard Biotools). Files were converted to FCS, randomized, and normalized for EQ bead intensity using the Helios software. Concatenating fcs files in the same group into one file was conducted by FlowJo v10.8 (BD Biosciences). Cytobank Premium (Cytobank Inc.) was used to perform manual gating, visualization of t-distributed stochastic neighbor embedding (viSNE), Uniform manifold approximation and projection (UMAP) analysis, and Citrus analysis (Bruggner et al., 2014).

Data analysis

Cisplatin-positive cells and doublets were excluded to select live cells, and $CD45^+$ cells were further analyzed. For T cells, $CD2^+$ $CD3^+$ cells were gated and subjected to UMAP and Citrus algorithms. The UMAP analysis included clustering channels for CD4, CD8a, CD27, CD28, CD45RA, CD45RO, Fas, and used the parameters: numbers of neighbors = 15, minimum distance = 0.01. The Citrus algorithm for T cells included clustering channels for CD4, CD5, CD7, CD8a, CD11a, CD16, CD27, CD28, CD44, CD45RA, CD45RO, CD49d, CD57, CD69, CD226, Fas, IL-2R, PD-L1, PD-L2, PD-1, OX40, TIGIT, TIM3, CTLA-4, CD223 (LAG-3), BTLA, ICOS, ST2, CCR7, CXCR3, HLA-DR, and used the parameters: association models = nearest shrunken centroid (PAMR), cluster characterization = abundance, minimum cluster size = 5%, cross validation folds = 5, false discovery rate = 1%. The citrus analysis excluded nivolumab-induced ILD cases due to the apparent loss of PD-1 detection caused by competitive inhibition by nivolumab (Supplementary Figure 1B) (Yanagihara et al., 2020). The viSNE analysis for T cells included clustering channels for CD4, CD5, CD7, CD8a, CD11a, CD16, CD27, CD28, CD44, CD45RA, CD45RO, CD49d, CD57, CD69, CD226, Fas, IL-2R, PD-L1, PD-L2, PD-1, OX40, TIGIT, TIM3, CTLA-4, CD223 (LAG-3), BTLA, ICOS, ST2, CCR7, CXCR3, and HLA-DR, and used the parameters: iterations = 1000, perplexity = 30, theta = 0.5.

For myeloid cells, $CD3^-$ $CD11b^+$ $CD11c^+$ cells were gated, and UMAP and Citrus algorithms were used. The UMAP analysis included clustering channels for CD11b, CD11c, CD64, CD14, CD16, CD206, HLA-DR, and CCR2, and used the parameters: numbers of neighbors = 10, minimum distance = 0.01. The Citrus algorithm included clustering channels for CD11b, CD11c, CD64, CD14, CD16, CD32, CD36, CD38, CD84, CD86, CD163, CD206, CD209, CD223, HLA-DR, CCR2, CCR5, and ST2, and used the parameters: association models = nearest shrunken centroid (PAMR), cluster

characterization = abundance, minimum cluster size = 5%, cross validation folds = 5, false discovery rate = 1%. One case of PCP was excluded from the Citrus analysis due to low cell numbers.

B cells and Plasma cells were identified using gating of $CD3^{-}CD64^{-}$ and $CD19^{+}$ or $CD138^{+}$ cells. viSNE analysis was performed to cluster B cells using the following markers: CD19, CD38, CD11c, IgA, IgG, CD138, CD21, ST2, CXCR5, CD24, CD27, TIM-1, IgM, HLA-DR, IgD, and FCRL5. The analysis was performed on both individual and concatenated files using the parameters of 1000 iterations, perplexity of 30, and theta of 0.5.

The selection of the dimensionality reduction technique, UMAP or viSNE, was made based on their ability to retain the relationships between global structures and the distances between cell clusters (where UMAP outperformed viSNE) and their ability to present a distinct and non-overlapping portrayal of cell subpopulations, facilitating the identification of inter-group variations (where viSNE performed better than UMAP).

Statistical analysis

We utilized a PAMR association model with a stringent threshold of 1% FDR, as described in the *Data Analysis* section, for the Citrus algorithm experiment. The Student's two-tailed unpaired t-test was employed to conduct a comparative analysis between the two groups. To determine the significance of serum beta-D-glucan and KL-6 among three groups, a statistical analysis was performed using Kruskal-Wallis tests. We evaluated the manually gated cell proportions by performing a two-way ANOVA, along with Tukey's multiple comparison tests. Data were analyzed using GraphPad Prism 9 software. Statistical significance was considered to be achieved when the P-value was less than 0.05.

Analysis of single-cell RNA sequencing data of human BALF cells

For our investigation, we utilized the publicly available dataset GSE145926, which contains single-cell RNA sequencing data from BALF cells of both healthy controls (n = 3) and patients with severe COVID-19 (n = 6) (Liao et al., 2020). We initiated our analysis by normalizing the filtered gene-barcode matrix using the 'NormalizeData' function in Seurat version 4, applying the default settings. Subsequently, we identified the top 2,000 variable genes utilizing the 'vst' method available in the 'FindVariableFeatures' function of Seurat. Principal Component Analysis (PCA) and UMAP were then conducted to reduce dimensionality and visualize the data. To isolate T

cells for further analysis, we defined them as cells expressing *CD2* and *CD3E* with expression values greater than 1. We specifically examined the expression of *FCGR3A* (CD16) by setting an expression threshold of 0.5 to identify relevant cell populations. The resulting expression patterns were illustrated using violin plots and bar plots, which were generated using the 'ggplot' function in R.

Results

Patient characteristics and clinical parameters

We analyzed 7 cases of PCP, 9 of DI-ILD, and 9 of ICI-ILD (Table 1). One of the PCP cases was fatal. Differential cell counts for BALF revealed lymphocytosis in 7 out of 7 cases (100%) of PCP as well as in 8 out of 9 cases (88.9%) of DI-ILD and 7 out of 9 cases (63.6%) of ICI-ILD when the cut-off for the percentage of lymphocytes was set to >20%. Serum levels of beta-D-glucan were significantly higher in patients with PCP than those with DI-ILD or ICI-ILD (196.5 ± 419.8, 3.7 ± 7.1, 0.6 ± 1.4 pg/mL, respectively) (Figure 2A). The receiver operating characteristic (ROC) curve was constructed to evaluate the diagnostic utility of beta-D-glucan for PCP, with values from the DI-ILD group used as a reference (Figure 2B). The area under the curve was determined to be 0.8929. When the cut-off value was set to 14.70 pg/mL, the sensitivity and specificity of PCP were 85.71% and 87.50%, and the positive likelihood ratio was 6.86. The diagnostic value of beta-D-glucan was consistent with the previous study (Tasaka et al., 2007), where the positive likelihood ratio was 6.57, with a cut-off value of 31.0. The serum levels of KL-6, an indicator of various types of interstitial pneumonitis (Ishikawa et al., 2012), tended to be higher in patients with ICI-ILD than PCP or DI-ILD, though insignificant (Figure 2C). Four out of 7 (57.1%) in PCP, 1 out of 9 (11.1%) in DI-ILD, and 6 out of 9 (66.7%) in ICI-ILD were positive for KL-6 with a cut-off value of 500 U/mL.

Expansion of CD16^{+}T cells in BALF from patients with PCP

First, we investigated whether subsets of T cells (gated CD2^{+} CD3^{+}) differentially existed in PCP, DI-ILD, and ICI-ILD with mass cytometry. T-cell lymphocytosis was observed in all groups (PCP: 62.9 ± 17.5%, DI-ILD: 58.3 ± 24.5%, ICI-ILD: 50.4 ± 29.9%) with a higher tendency of CD4/CD8 ratio observed in DI-ILD compared to PCP and ICI-ILD (PCP: 1.13 ± 0.86, DI-ILD: 6.08 ± 6.06, ICI-ILD: 1.9 ± 1.40)(Figure 3A). To visualize T cell differentiation within the affected lungs, we generated UMAP plots (Figure 3B). The majority of T cells in the BALF displayed either memory or effector

phenotypes, with a limited population of naïve T cells (Figures 3B and 3C). Specifically, we observed a tendency of a higher abundance of transient memory/ effector memory CD4 T cells and a lower abundance of transient memory/ effector memory CD45RA (EMRA) CD8 T cells in DI-ILD compared to the other two groups (Figure 3C).

We then utilized the Citrus algorithm to classify T cell subpopulations with varying degrees of abundance in an unsupervised manner by analyzing 31 parameters (Figure 3D, Supplementary Figures 1C and 1D). Our analysis identified 30 clusters of T cells, of which 13 were significantly differentiated between the groups. Interestingly, clusters #26299, #26293, and #26278, characterized by $CD8^+$ T cells expressing CD16 (FcγRIIIa), and cluster #26286, characterized by $CD4^+$ T cells expressing CD16, were abundant in PCP compared to DI-ILD and ICI-ILD (Figures 3E and 3F). These $CD8^+$ T cells expressing CD16 were also positive for HLA-DR and CXCR3 (Figure 3F) but negative for CD14, a marker for monocytes (median CD14 expression of these clusters: 0.0–0.1 vs. 7.4–9.5 in monocyte populations). Cluster #26303, prevalent in ICI-ILD, comprised $CD8^+$ $CD57^+$ $TIGIT^+$ $LAG3^+$ but $CD16^-$ subpopulation (Figures 3E and 3F). These cells also expressed PD-1 and TIM-3, although the expression was lower than clusters #26299, #26293, and #26278. These $CD8^+$ T cells expressed CD45RA but no expression of CD45RO and CCR7, indicating EMRA phenotype. Cluster #26281, prevalent in DI-ILD, was marked by $CD4^+$ with low immune checkpoint expression (PD-1, TIM-3, TIGIT, LAG3, PD-L1, PD-L2, and OX40; Figures 3E and 3F).

Myeloid cell subpopulations in the lungs of PCP, DI-ILD, and ICI-ILD

Next, we investigated myeloid cell populations (identified as $CD3^-$ $CD11b^+$ $CD11c^+$). We first conducted UMAP to see the major myeloid cell populations. The UMAP plot categorized four major subtypes: monocytes, $CCR2^+$ macrophages, alveolar macrophages, and dendritic cells, with no significant difference in PCP, DI-ILD, and ICI-ILD (Figures 4A and 4B). We next utilized the Citrus algorithm to further investigate differently abundant myeloid cell subpopulations by analyzing 18 parameters. Our analysis identified 31 clusters of myeloid cells, of which 17 were significantly differentiated between the groups (Figure 4C, Supplementary Figure 2). Clusters #8220, #8215, and #8195, prevalent in PCP, were comprised of $CD11b^{hi}$ $CD11c^{hi}$ $CD64^+$ $CD206^+$ alveolar macrophages with $HLA\text{-}DR^{hi}$ (Figures 4D and 4E). Clusters #8219 and #8197, prevalent in ICI-ILD, were characterized by $CD14^+$ $CCR2^+$ $CCR5^+$ monocyte subpopulations (Figures 4D and 4E). Clusters #8227, #8223, and #8208, prevalent in

DI-ILD, were marked by CD11b^{lo} CD11c^{lo} CD64^{lo} CCR5^{+} subpopulations (Figures 4D and 4E).

B cell subpopulations in the lungs of ILDs

In addition to T cells and myeloid cells, we sought to investigate whether there were differential representations of B cells in BALF from PCP, DI-ILD, and ICI-ILD. By utilizing CD45^{+}CD3^{-}CD64^{-} and CD19^{+} or CD138^{+} as gating parameters, we were able to detect the presence of B cells and plasma cells. The frequency of B cells/ plasma cells was found to be relatively higher in patients with PCP compared to the other two groups, although the proportion of B cells and plasma cells remained low in all groups. (Figure 5A). A t-SNE analysis of 17 parameters among B cells/plasma cells revealed the presence of various B cell subpopulations, including IgD^{+} naïve B cells, IgM^{+} B cells, IgG^{+} B cells, IgA^{+} B cells, plasmablasts, and plasma cells (Figure 5B). Although not significant, higher levels of IgG^{+} B cells were observed in patients with PCP, while individuals with ICI-ILD exhibited a greater presence of plasma cells (Figure 5C). Previous research has suggested that FCRL5^{+} B cells contribute to the pathogenesis of autoimmune disorders (Owczarczyk et al., 2020)(Dement-Brown et al., 2012). Therefore, we investigated the frequency of these cells in our study and found that FCRL5^{+} B cells were more abundant in patients with ICI-ILD compared to those with PCP and DI-ILD, suggesting these FCRL5^{+} B cells may have a role in irAE (8.37 ± 6.74%, 1.37 ± 2.30%, 2.29 ± 3.81%, respectively) (Figure 5D).

Marked CD16+ T cell expansion in BALF from a fatal case of PCP

One case of PCP that developed during the use of immunosuppressive drugs after living donor liver transplantation had a fatal course despite intensive treatment. Upon admission, chest CT images revealed the emergence of diffuse ground glass opacities and infiltration in the bilateral lungs (Figure 6A). The serum levels of beta-D-glucan and KL-6 were highly elevated (1,146 pg/mL and 1,561 U/mL, respectively). The T cell percentage was 51.3%, and the CD4/CD8 ratio was 0.58, which was not particularly different from other PCP cases (Figure 6B). Strikingly, 97.5% of T cells expressed CD16 in the BALF from the fatal case (Figures 6C and 6D). Further, not only the proportion but the CD16 intensity was the highest in the fatal case among PCP cases (Figure 6E). On the contrary, there did not appear to be any significant differences in myeloid cell fractions, and CD16 expression was not particularly high in the fatal case (Figure 6F). The correlation matrix of clinical parameters and mass cytometry parameters revealed that

CD16 intensity in T cells may be correlated with disease severity (r = 0.748, p = 0.053) and beta-D-glucan (r = 0.868, p = 0.011) (Figure 6G). Therefore, CD16 expression in T cells is not only a characteristic of PCP but also a potential indicator of disease severity. For reference, we investigated CD16 expression in BALF T cells from healthy controls along with severe COVID-19 patients using the publicly available single-cell RNA sequencing data (GSE145926). In the BALF of healthy controls, *FCGR3A* (CD16) expression was observed in 18.7% of $CD4^+$ T cells and 7.22% of $CD8^+$ T cells in healthy controls. In contrast, severe COVID-19 patients exhibited expression rates of 17.2% in CD4+ T cells and 22.1% in $CD8^+$ T cells (Figures 6H and 6I). Notably, $CD8^+$ T cells from COVID-19 patients showed significantly higher *FCGR3A* (CD16) expression compared to those from healthy controls (0.31 ± 0.62 vs 0.12 ± 0.43, p = 2.47e-08), while no significant difference was observed in $CD4^+$ T cells between the two groups (0.22 ± 0.53 vs 0.34 ± 0.73, p = 0.407).

Discussion

Here, we have demonstrated the characteristic immune cell subpopulations present in BALF from patients with PCP, DI-ILD, and ICI-ILD. Our analysis revealed an expansion of $CD16^+$ T cells in patients with PCP, an increase in $CD57^+$ $CD8^+$ T cells expressing immune checkpoints, and $FCRL5^+$ B cells in ICI-ILD.

CD16 is a low-affinity Fc receptor (FcγRIIIa) for IgG, commonly expressed on NK cells as well as on neutrophils and monocytes (Ravetch and Bolland, 2001), with only a small fraction of T cells expressing CD16 in healthy peripheral blood (Sandor and Lynch, 1993) and BALF (Figures 6H and 6I). On the contrary, $CD16^+$ T cells are induced in specific conditions, such as chronic hepatitis C infection (Björkström et al., 2008) and COVID-19 (Georg et al., 2022). In chronic hepatitis C infection, $CD16^+$ CD8 T cells displayed a late-stage effector phenotype with high levels of perforin with a restricted TCR profile (Björkström et al., 2008). Stimulation of CD16 on CD8 T cells evokes a vigorous response such as degranulation and cytokine production (IFN-γ and TNF-α) similar to that of CD16 stimulation in NK cells (Björkström et al., 2008). These $CD16^+$ $CD8^+$ T cells also express a senescent marker, CD57, which differs from our findings that expanding $CD16^+$ CD8 T cells in PCP did not express CD57 (Figure 3F).

Georg *et al.* recently discovered that COVID-19 severity was associated with highly activated $CD16^+$ T cells, which exhibit increased cytotoxic functions (Georg et al., 2022). Although this increase was observed in $CD8^+$ T cells and not in $CD4^+$ T cells, the augmented population of $CD16^+$ T cells in BALF from patients with severe COVID-19

was further substantiated by data mining of scRNA-seq (Figures 6H and 6I). CD16 expression allows T cells to degranulate and exert cytotoxicity in an immune-complex-mediated, TCR-independent manner. Moreover, $CD16^+$ T cells from COVID-19 patients caused injury to microvascular endothelial cells and induced the release of neutrophil and monocyte chemoattractants (Georg et al., 2022). Georg *et al.* also discovered that severe COVID-19 induced increased generation of C3a, which further activates $CD16^+$ cytotoxic T cells. The proportions of activated $CD16^+$ T cells and plasma levels of complement proteins upstream of C3a were found to be associated with fatal outcomes of COVID-19, proving support for the pathological role of exacerbated cytotoxicity and complement activation in COVID-19 (Georg et al., 2022). Given these findings and the observation of the highest proportion of $CD16^+$ T cells in the fatal case of PCP, we hypothesize that these $CD16^+$ T cells may possess excessive cytotoxicity toward pulmonary microvascular endothelial cells, contributing to lung injury in PCP, in addition to targeting *Pneumocystis jirovecii*. Based on the therapeutic efficacy of an anti-complement therapy (anti-C5a antibody) for severe COVID-19 (Campbell, 2020)(Vlaar et al., 2020), anti-complement treatments may have the potential to treat severe PCP. One of the other T cell markers correlated with the severity of PCP was CCR7, CD7, and CD57 (Supplementary Figure 4), although the precise biological significance of the correlation remains to be elucidated.

We discovered an increase of $CD57^+$ $CD8^+$ T cells expressing immune checkpoints, PD-1^+ $TIGIT^+$ $LAG3^+$ TIM-3^+ in ICI-ILDs, which supports our previous findings of increased proportions of $CD8^+$ T cells positive for both PD-1 and TIM-3 or TIGIT in ICI-ILD (Suzuki et al., 2020). In the methods section, the low detection of PD-1 expression on T cells in patients treated with nivolumab was noted; this was due to the competitive nature of the PD-1 detection antibody EH12.2 with nivolumab (Yanagihara et al., 2020). The absence of a metal-conjugated PD-1 antibody with the MIH4 clone presented a limitation in our study. Ideally, we would have conjugated the MIH4 antibody with 155Gd for our analysis, which is a refinement we aim to incorporate in future research. A population of PD-1^+ TIM-$3^+$$CD8^+$ cells was detected in the peritumoral pleural effusion and ILD lesions of a cancer patient undergoing ICI treatment (Yanagihara et al., 2017). Through the application of next-generation sequencing technology to the DNA encoding the complementarity-determining region of the T-cell receptor (TCR), identical T-cell clones were identified in both peritumoral pleural effusion and ILD lesions (Tanaka et al., 2018). Similar to ICI-ILD, a recent study identified T cells specific to α-myosin drive ICI-related myocarditis (Axelrod et al.,

2022). These results indicate that ICI-activated $CD8^+$ T cells, with a phenotype of $PD\text{-}1^+$ $TIGIT^+$ $LAG3^+$ $TIM\text{-}3^+$, could potentially trigger ILD by recognizing self-peptides or shared epitopes between tumors and lungs. $CD16^+$ $CD8^+$ T cells in PCP exhibit high CXCR3 and ST2 expression, and $CD57^+$ $CD8^+$ T cells expressing immune checkpoints in ICI-ILD express high CXCR3 (consistent with the previous study (Kim et al., 2021)). Therefore, these $CD8^+$ T cells could potentially migrate into the lungs via chemokines, such as CXCL4, CXCL9, CXCL10, and IL-33 (Van Raemdonck et al., 2015)(Griesenauer and Paczesny, 2017).

Regarding CD57 expression in T cells, it is generally considered a senescent marker (Fehlings et al., 2022). However, $CD57^+$ $CD8^+$ T cells in the periphery show clonal expansion with the overlap of the TCR repatoire of tumor-infiltrating T cells with favorable response to ICI in patients with cancer (Fehlings et al., 2022), indicating these $CD57^+$ $CD8^+$ T cells may have a highly active phenotype in ICI-treated individuals.

FCRL5 is a B cell-restricted member of the Fc receptor-like family encoded by the *IRTA2* gene (Rostamzadeh et al., 2018). In both rheumatoid arthritis (Owczarczyk et al., 2011) and granulomatosis with polyangiitis and microscopic polyangiitis (Owczarczyk et al., 2020), increased expression of FCRL5 was indicative of a positive response to rituximab. Additionally, our recent research revealed an increase in $FCLR5^+$ B cells in connective-tissue disease-related ILD (Hata et al., 2023). These findings suggest a potential pathological role of FCRL5 in autoimmunity. Given that ICI-ILD is considered a type of irAE, it is reasonable to hypothesize that $FCRL5^+$ B cells may be one of the immune cells associated with autoimmunity.

Regarding myeloid cells, we found that $CD14^+$ $CCR2^+$ $CCR5^+$ monocyte subpopulations were prevalent in ICI-ILD. Franken *et al.* revealed a decrease in anti-inflammatory resident alveolar macrophages and an increase in pro-inflammatory 'M1-like' monocytes (expressing TNF, IL-1B, IL-6, IL-23A, and GM-CSF receptor CSF2RA, CSF2RB) in BALF from ICI-ILD compared with controls (Franken et al., 2022). Taken together with this report, the $CD14^+$ $CCR2^+$ $CCR5^+$ monocytes we found may be an M1-like monocyte.

Our study has several limitations, including the absence of data from healthy individuals, a relatively small sample size, and a retrospective design that resulted in missing clinical data for certain cases. Selection bias may also be a factor, as only patients who underwent bronchoalveolar lavage were eligible for enrollment in this study. It is important to note that these findings demonstrate a correlation rather than proof of causation.

In summary, our study has shown distinct immune cell phenotypes in PCP, DI-ILD, and ICI-ILD. Specifically, we have identified an expansion of $CD16^+$ T cells in PCP, as well as an increase in $CD57^+$ $CD8^+$ T cells expressing immune checkpoints, $FCRL5^+$ B cells, and $CCR2^+$ $CCR5^+$ monocytes in ICI-ILD, which may play a pathogenic role. Based on these findings, further confirmatory research may lead to the development of diagnostic methods and novel strategies that target these specific cell populations to treat chemotherapy-induced pneumonitis.

Author contributions

Conceptualization: TY; Methodology: KH, TY, KM, KK, and YB; Investigation: KH, TY, KM, KK, KS, KT, DE, HA, and MU; Visualization: KH, TY, KM, KK, KS, KT, DE, HA, MU, SI, and YB; Funding acquisition: TY and YF; Supervision: SI, YB, YF, and IO; Writing-original draft: KH and TY; Writing-review and editing: SI, YB, YF, and IO. All authors contributed to the article and approved the submitted version.

Acknowledgments

We thank Ms. Sanae Sekihara, PhD. from Standard Biotools, for her technical assistance. We also extend our appreciation to the Medical Research Center Initiative for High Depth Omics at Kyushu University.

Funding

This research was supported by the Kakihara Foundation, and Boehringer Ingelheim (T.Y.), and the Japan Agency for Medical Research and Development (Y.F.).

Table 1. Characteristics of the study population.

	PCP	DI-ILD	ICI-ILD
Number	7	9	9
Age	66.9±4.6	58.8±19.3	71.9±4.5
Male %	42.8(3)	77.8(7)	100(9)
Suspected drug/regimen		VAC (2), FOLFIRI(2), DTX(1), AC(1), GEM(1), TS-1(1), BEP(1)	Nivolumab (3), Pembrolizumab (3), Durvalmab (2), Atezolizumab (1)
CTCAE grade	G2(5), G3(1), G5(1)	G1(2), G2(7)	G2(7), G3(2)
BALF cell differentiation (%)			
Macrophage	25±8.9	40.2±23.5	44.4±26.6
Neutrophil	13.6±29.7	1.9±1.3	14.4±26.7
Lymphocyte	58.8±30.5	56.2±24.8	35.6±23.7
Eosinophil	0.9±1.1	1.7±1.9	5.6±8.5

Data for age and BALF analysis are presented as means ± SD. PCP: *Pneumocystis jirovecii* pneumonia, DI-ILD: cytotoxic drug-related interstitial lung disease, ICI-ILD: immune-checkpoint inhibitor-related ILD, BALF: bronchoalveolar lavage fluid.
VAC: vincristine, actinomycin D, and cyclophosphamide; FOLFIRI: folinic acid, fluorouracil, and irinotecan hydrochloride; DTX: docetaxel, AC: Adriamycin and cyclophosphamide; GEM: gemcitabine; TS-1: Tegafur Gimeracil Oteracil Potassium; BEP: bleomycin, etoposide, and platinum.
Common Terminology Criteria evaluated the severity of the disease for Adverse Events (CTCAE) grading. Grade 1: asymptomatic, grade 2: symptomatic, grade 3: severe symptoms, requiring oxygen therapy, grade 4: life-threatening respiratory failure, grade 5: death.

Figure Legends

Figure 1. Graphical abstract of the study.

Bronchoalveolar lavage fluid (BALF) samples were collected from patients with *Pneumocystis jirovecii* pneumonia (PCP), cytotoxic drug-induced interstitial lung disease (DI-ILD), and immune-checkpoint inhibitor-related ILD (ICI-ILD). Subsequently, BALF cells were analyzed using mass cytometry with a T cell panel (35 markers) and B cell/myeloid cell panel (32 markers) following CD45 barcoding for sample identification. The study found that there was a significant increase in the expansion of $CD16^{+}$ T cells in patients with PCP, with the highest CD16 expression observed in a fatal case of PCP.

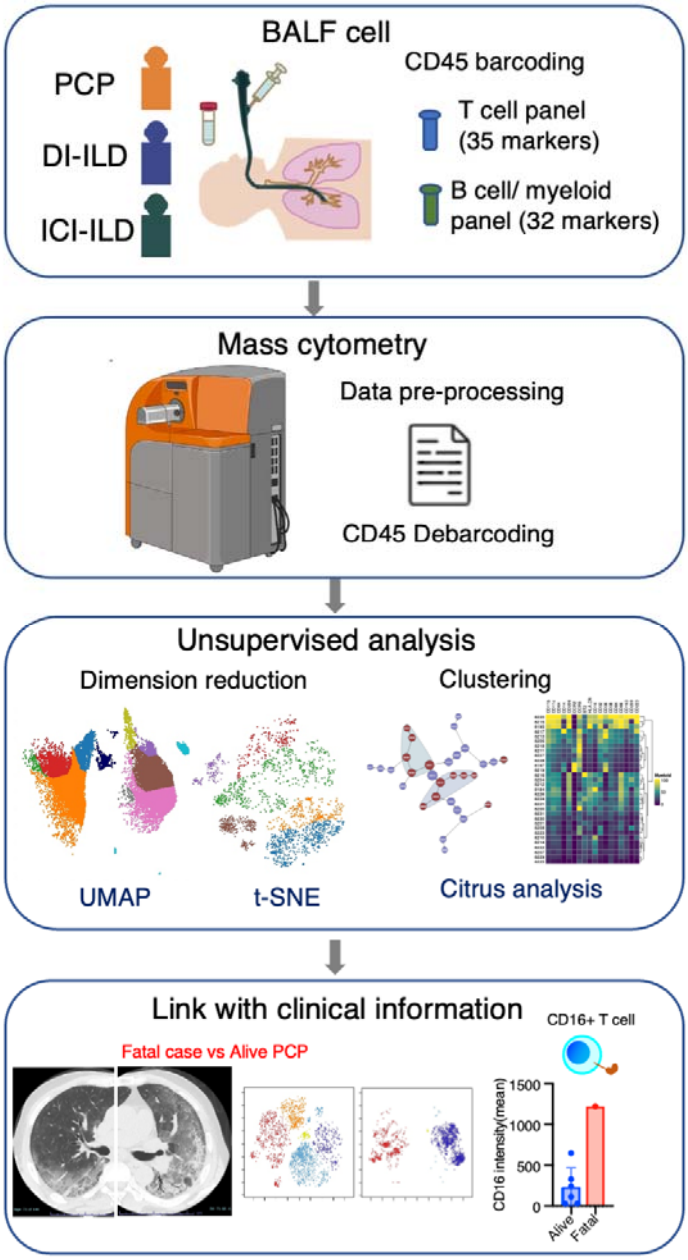

Figure 2. Serum levels of beta-D-glucan and KL-6 from patients with PCP, DI-ILD, and ICI-ILD.

(A) Serum levels of beta-D-glucan from patients with Pneumocystis jirovecii pneumonia (PCP), cytotoxic drug-related interstitial lung disease (DI-ILD), and immune-checkpoint inhibitor-related ILD (ICI-ILD). (B) A receiver operating characteristic (ROC) curve was constructed to evaluate the diagnostic utility of beta-D-glucan for PCP, with values from the DI-ILD group used as a reference. The area under the curve was determined to be 0.8929. (C) Serum levels of KL-6.

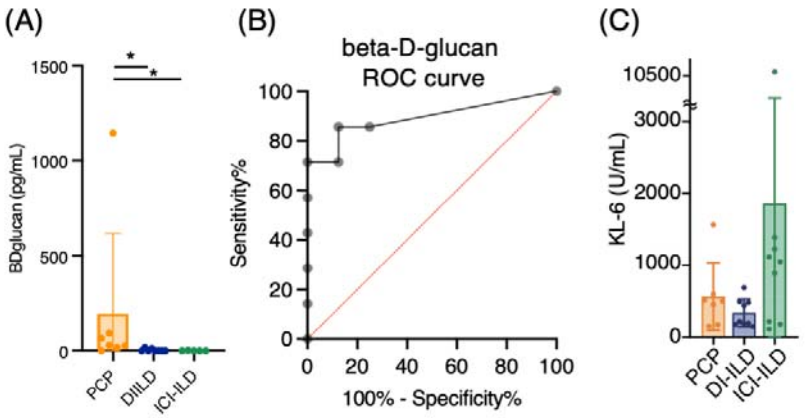

Figure 3. Characterization of T cell subsets in BALF from patients with PCP, DI-ILD, and ICI-ILD.

(A) Percentage of T cells (defined as $CD2^{+}CD3^{+}$) in $CD45^{+}$ BALF cells and CD4/CD8 ratio in T cells from patients with *Pneumocystis jirovecii* pneumonia (PCP), cytotoxic drug-related interstitial lung disease (DI-ILD), and immune-checkpoint inhibitor-related ILD (ICI-ILD). (B) Uniform manifold approximation and projection (UMAP) of concatenated samples visualizing the distribution of T cell subpopulations. Central memory (CM) T cells were defined by $CCR7^{+}$ $CD45RO^{+}$ $CD28^{+}$ Fas^{+}, Transitional memory (TM) by $CCR7^{-}$ $CD45RO^{+}$ $CD28^{+}$ Fas^{+}, Effector memory (EM) by $CCR7^{-}$ $CD45RO^{+}$ $CD28^{-}$ Fas^{+}, Terminal effector (TE) by $CCR7^{-}$ $CD45RO^{+/-}$ Fas^{-}, Effector memory RA (EMRA) by $CCR7^{-}$ $CD45RO^{-}$ $CD45RA^{+}$ $Fas^{+/-}$. Arrows indicate the trajectory of T-cell differentiation. DN: $CD4^{-}$ $CD8^{-}$ double negative, DP: $CD4^{+}$ $CD8^{+}$ double positive. (C) Percentage of T cell subpopulations. (D) Citrus network tree visualizing the hierarchical relationship of each marker between identified T cell populations gated by $CD45^{+}CD2^{+}$ $CD3^{+}$ from PCP (n = 7), DI-ILD (n = 9), and ICI-ILD (n = 5). Clusters with significant differences were represented in red, and those without significant differences in blue. Circle size reflects the number of cells within a given cluster. (E) Citrus-generated violin plots for six representative and differentially regulated populations. Each cluster number (#) corresponds to the number shown in panel (D). (F) Heatmap demonstrates the expression of various markers in different clusters of T cells, as identified through the Citrus analysis. All differences in abundance were significant at a false discovery rate < 0.01.

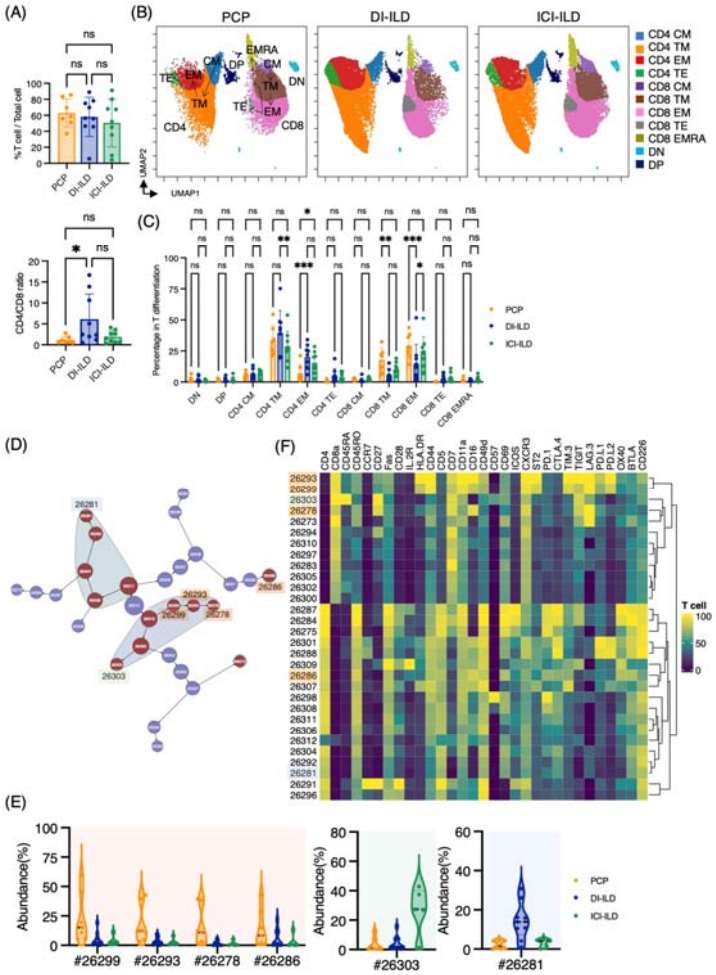

Figure 4. Characterization of myeloid cell subsets in BALF from patients with PCP, DI-ILD, and ICI-ILD.

(A) UMAP of concatenated samples visualizing the distribution of myeloid cell sub-populations in $CD3^{-}$ $CD11b^{+}$ $CD11c^{+}$ gated myeloid cells in BALF from patients with *Pneumocystis jirovecii* pneumonia (PCP), cytotoxic drug-related interstitial lung disease (DI-ILD), and immune-checkpoint inhibitor-related ILD (ICI-ILD). Monocytes were defined by $CD64^{+}$ $CD14^{+}$, $CCR2^{+}$ macrophages (Mp) by $CD64^{+}$ $CD14^{-}$ $CCR2^{+}$, Alveolar Mp by $CD64^{+}$ $CD14^{-}CCR2^{-}$ $CD206^{+}$, dendritic cells (DC) by $CD64^{-}CD14^{-}CD206^{-}CD11c^{+}$ $HLA\text{-}DR^{+}$, Unidentified subsets by $CD64^{-}$ $CD11b^{+/-}$ $CD11c^{+/-}$ $CD14^{-}$ $CD206^{-}$. (B) Percentage of myeloid cell sub-populations in PCP (n = 7), DI-ILD (n = 9), and ICI-ILD (n = 9). Dot plots represent individual samples. (C) Citrus network tree visualizing the hierarchical relationship of each marker between identified myeloid cell populations gated by $CD45^{+}$ $CD3^{-}$ $CD11b^{+}$ $CD11c^{+}$ from PCP (n = 6), DI-ILD (n = 9), and ICI-ILD (n = 9). Clusters with significant differences were represented in red, and those without significant differences in blue. Circle size reflects the number of cells within a given cluster. (D) Citrus-generated violin plots for six representative and differentially regulated populations. Each cluster number (#) corresponds to the number shown in panel (C). All differences in abundance were significant at a false discovery rate < 0.01. (E) Heatmap demonstrates the expression of various markers in different clusters of myeloid cells, as identified through the Citrus analysis.

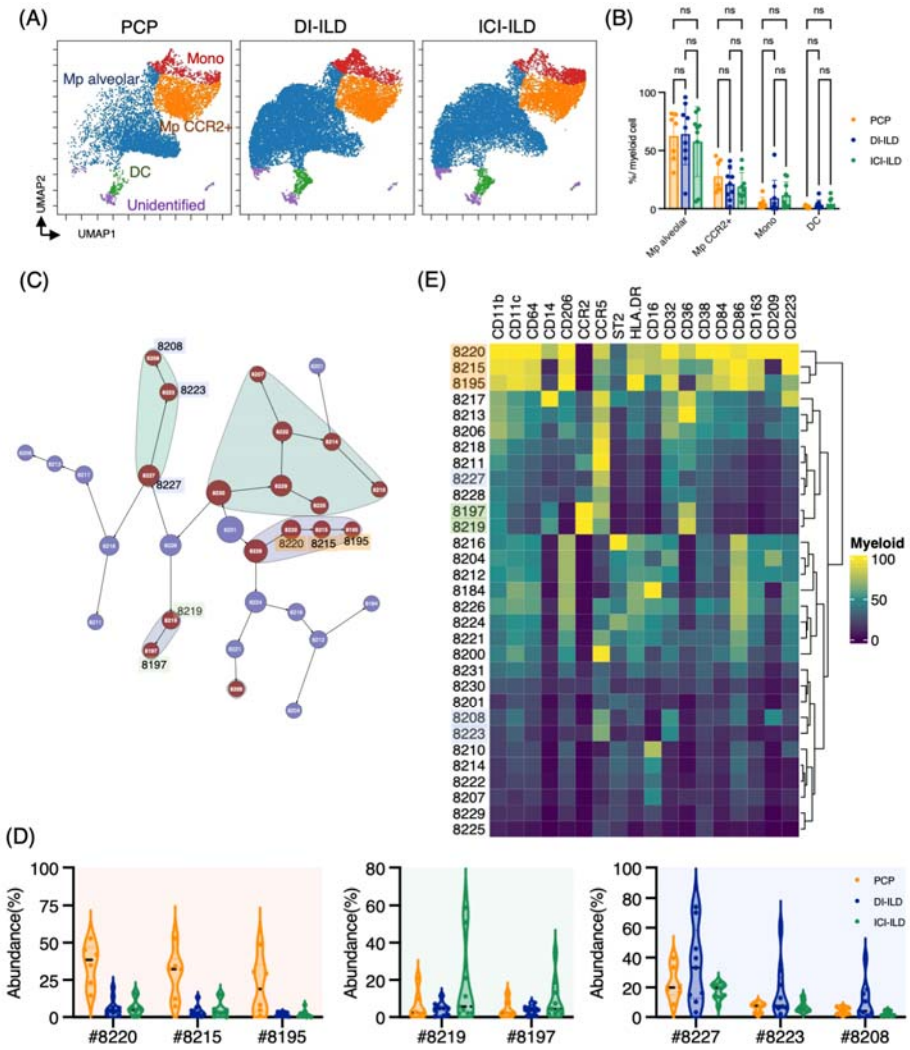

Figure 5. Characterization of B cell subsets in BALF from patients with PCP, DI-ILD, and ICI-ILD.

(A) Percentages of B cells and plasma cells in $CD45^+$ BALF cells. (B) t-stochastic neighborhood embedding (t-SNE) plots of concatenated samples visualizing the distribution of B cell subpopulations in $CD64^-CD3^-$ and $CD19^+$ or $CD138^+$ gated B cells in BALF from patients with PCP, DI-ILD, and ICI-ILD. Naive B cells are defined by $CD19^+IgD^+$, IgM B cells: $CD19^+$ IgM^+, IgG B cells: $CD19^+$ IgG^+, IgA B cells: $CD19^+$ IgA^+, plasmablasts: $CD19^+$ $CD27^+$ $CD38^+$ $CD138^-$, plasma cells: $CD19^-$ $CD138^+$ and IgG^+ or IgA^+. (C) Percentages of B cell subpopulations in PCP (n = 7), DI-ILD (n = 9), and ICI-ILD (n = 9). Dot plots represent individual samples. (D) Two-dimensional dot plots depicting FCRL5-expressing B cells within a gated population of B cells defined as $CD64^-CD3^-$ and $CD19^+$ or $CD138^+$. Percentages of FCRL5-expressing B cells within the total B cell population are also shown.

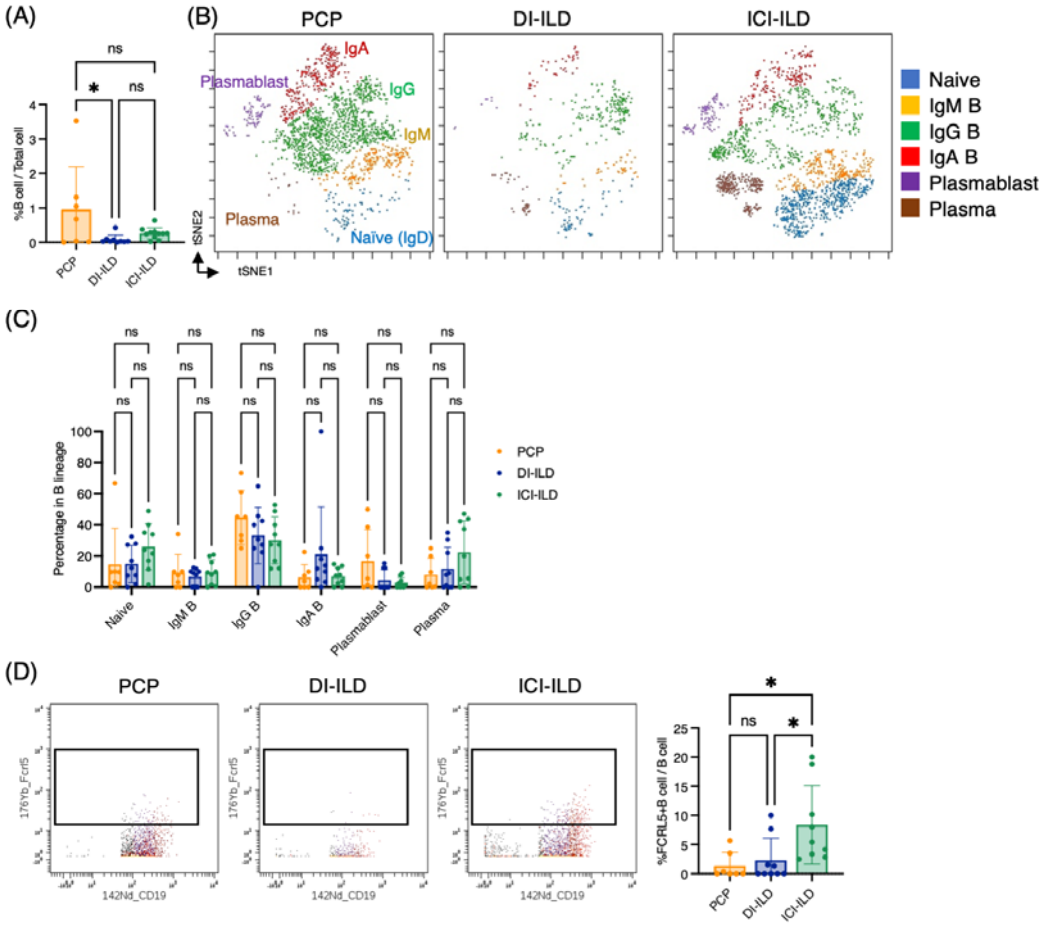
(A)
ns
*
ns
%B cell / Total cell
PCP
DI-ILD
ICI-ILD
(B)
PCP
DI-ILD
ICI-ILD
IgA
Plasmablast
IgG
IgM
Plasma
Naïve (IgD)
tSNE2
tSNE1
Naive
IgM B
IgG B
IgA B
Plasmablast
Plasma
(C)
Percentage in B lineage
PCP
DI-ILD
ICI-ILD
Naive
IgM B
IgG B
IgA B
Plasmablast
Plasma
(D)
PCP
DI-ILD
ICI-ILD
176Yb_Fcrl5
142Nd_CD19
%FCRL5+B cell / B cell
ns
*
*
PCP
DI-ILD
ICI-ILD

Figure 6. Immunological phenotypes in a fatal case of PCP.
(A) Chest computed tomography images of the patient upon admission reveal the emergence of bilateral diffuse ground glass opacities and infiltration in both lungs. (B) Comparison of T cell percentage and CD4/CD8 ratio between a fatal case and surviving cases of PCP. (C) t-SNE plots illustrating the distribution of T cell subpopulations in BALF T cells (gated as $CD45^{+}CD2^{+}CD3^{+}$) from a fatal case and surviving cases of PCP. Double negative (DN) T cells were defined as $CD4^{-}CD8^{-}$ T cells. (D) Percentages of each T-cell subpopulation. Red dots represent the value of the fatal case. (E) Mean CD16 intensity in the T cell population. (F) Mean CD16 intensity in the myeloid cell population. (G) The correlation matrix in PCP cases. Pearson *r* values are shown in each square. (H) Violin plots illustrate *FCGR3A* (CD16) expression intensity on $CD4^{+}$ and $CD8^{+}$ T cells, with each dot representing an individual cell in bronchoalveolar lavage fluid (BALF) from healthy controls (HC) and COVID-19 patients, derived from single-cell RNA-seq dataset GSE145926. The significance of differences was assessed using the Wilcoxon test. ns: not significant, *** $p < 0.001$. (I) The proportion of *FCGR3A* (CD16)-positive cells within the $CD4^{+}$ and $CD8^{+}$ T cell populations in BALF from HC and COVID-19 patients, with the *FCGR3A* expression threshold set at 0.5.

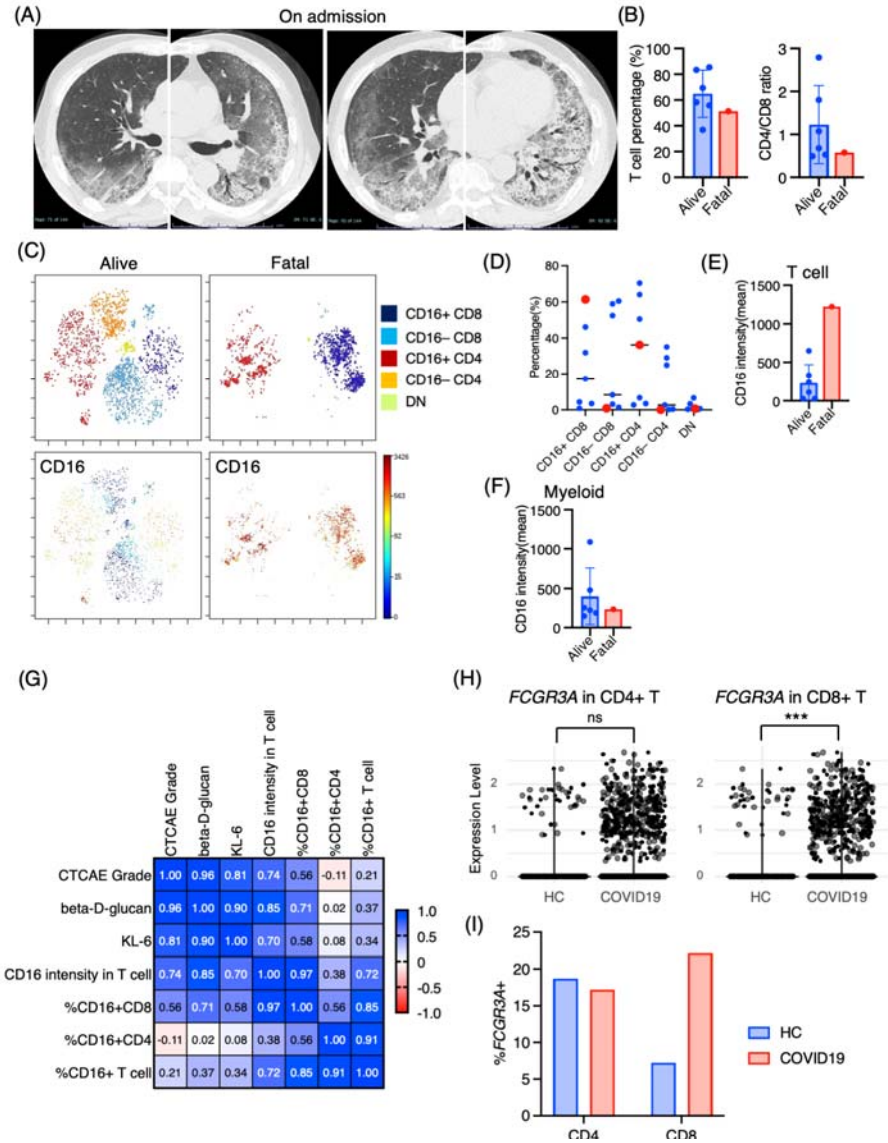

Reference

Ando H, Suzuki K, Yanagihara T. 2021. Insights into Potential Pathogenesis and Treatment Options for Immune-Checkpoint Inhibitor-Related Pneumonitis. *Biomedicines* **9**:1484. doi:10.3390/biomedicines9101484

Apostolopoulou A, Fishman JA. 2022. The Pathogenesis and Diagnosis of Pneumocystis jiroveci Pneumonia. *J Fungi* **8**. doi:10.3390/jof8111167

Asai N, Motojima S, Ohkuni Y, Matsunuma R, Nakashita T, Kaneko N, Mikamo H. 2022. Pathophysiological mechanism of non-HIV Pneumocystis jirovecii pneumonia. *Respir Investig* **60**:522–530. doi:10.1016/j.resinv.2022.04.002

Axelrod ML, Meijers WC, Screever EM, Qin J, Carroll MG, Sun X, Tannous E, Zhang Y, Sugiura A, Taylor BC, Hanna A, Zhang S, Amancherla K, Tai W, Wright JJ, Wei SC, Opalenik SR, Toren AL, Rathmell JC, Ferrell PB, Phillips EJ, Mallal S, Johnson DB, Allison JP, Moslehi JJ, Balko JM. 2022. T cells specific for α-myosin drive immunotherapy-related myocarditis. *Nature* **611**:818–826. doi:10.1038/s41586-022-05432-3

Björkström NK, Gonzalez VD, Malmberg K, Falconer K, Alaeus A, Nowak G, Jorns C, Ericzon B, Weiland O, Sandberg JK, Ljunggren H-G. 2008. Elevated numbers of Fc gamma RIIIA+ (CD16+) effector CD8 T cells with NK cell-like function in chronic hepatitis C virus infection. *J Immunol* **181**:4219–28. doi:10.4049/jimmunol.181.6.4219

Bruggner R V, Bodenmiller B, Dill DL, Tibshirani RJ, Nolan GP. 2014. Automated identification of stratifying signatures in cellular subpopulations. *Proc Natl Acad Sci U S A* **111**:E2770-7. doi:10.1073/pnas.1408792111

Campbell CM. 2020. The opening salvo of anti-complement therapy against COVID-19. *Lancet Rheumatol* **2**:e729–e730. doi:10.1016/S2665-9913(20)30353-2

Chedid C, Andrieu T, Kokhreidze E, Tukvadze N, Biswas S, Ather MF, Uddin MKM, Banu S, De Maio F, Delogu G, Endtz H, Goletti D, Vocanson M, Dumitrescu O, Hoffmann J, Ader F. 2022. In-Depth Immunophenotyping With Mass Cytometry During TB Treatment Reveals New T-Cell Subsets Associated With Culture Conversion. *Front Immunol* **13**:1–16. doi:10.3389/fimmu.2022.853572

Conte P, Ascierto PA, Patelli G, Danesi R, Vanzulli A, Sandomenico F, Tarsia P, Cattelan A, Comes A, De Laurentiis M, Falcone A, Regge D, Richeldi L, Siena S. 2022. Drug-induced interstitial lung disease during cancer therapies: expert opinion on diagnosis and treatment. *ESMO Open* **7**:100404. doi:10.1016/j.esmoop.2022.100404

Couloume L, Ferrant J, Le Gallou S, Mandon M, Jean R, Bescher N, Zephir H, Edan G, Thouvenot E, Ruet A, Debouverie M, Tarte K, Amé P, Roussel M, Michel L. 2021. Mass Cytometry Identifies Expansion of T-bet+ B Cells and CD206+ Monocytes in Early Multiple Sclerosis. *Front Immunol* **12**:1–12. doi:10.3389/fimmu.2021.653577

Delaunay M, Prévot G, Collot S, Guilleminault L, Didier A, Mazières J. 2019. Management of pulmonary toxicity associated with immune checkpoint inhibitors. *Eur Respir Rev* **28**:4–13. doi:10.1183/16000617.0012-2019

Dement-Brown J, Newton CS, Ise T, Damdinsuren B, Nagata S, Tolnay M. 2012. Fc receptor-like 5 promotes B cell proliferation and drives the development of cells displaying switched isotypes. *J Leukoc Biol* **91**:59–67. doi:10.1189/jlb.0211096

Fehlings M, Kim L, Guan X, Yuen K, Tafazzol A, Sanjabi S, Zill OA, Rishipathak D, Wallace A, Nardin A, Ma S, Milojkovic A, Newell EW, Mariathasan S, Yadav M. 2022. Single-cell analysis reveals clonally expanded tumor-associated CD57 +CD8 T cells are enriched in the periphery of patients with metastatic urothelial cancer responding to PD-L1 blockade. *J Immunother Cancer* **10**:1–13. doi:10.1136/jitc-2022-004759

Franken A, Van Mol P, Vanmassenhove S, Donders E, Schepers R, Van Brussel T, Dooms C, Yserbyt J, De Crem N, Testelmans D, De Wever W, Nackaerts K, Vansteenkiste J, Vos R, Humblet-Baron S, Lambrechts D, Wauters E. 2022. Single-cell transcriptomics identifies pathogenic T-helper 17.1 cells and pro-inflammatory monocytes in immune checkpoint inhibitor-related pneumonitis. *J Immunother cancer* **10**. doi:10.1136/jitc-2022-005323

Georg P, Astaburuaga-García R, Bonaguro L, Brumhard S, Michalick L, Lippert LJ, Kostevc T, Gäbel C, Schneider M, Streitz M, Demichev V, Gemünd I, Barone M, Tober-Lau P, Helbig ET, Hillus D, Petrov L, Stein J, Dey H-P, Paclik D, Iwert C, Mülleder M, Aulakh SK, Djudjaj S, Bülow RD, Mei HE, Schulz AR, Thiel A, Hippenstiel S, Saliba A-E, Eils R, Lehmann I, Mall MA, Stricker S, Röhmel J, Corman VM, Beule D, Wyler E, Landthaler M, Obermayer B, von Stillfried S, Boor P, Demir M, Wesselmann H, Suttorp N, Uhrig A, Müller-Redetzky H, Nattermann J, Kuebler WM, Meisel C, Ralser M, Schultze JL, Aschenbrenner AC, Thibeault C, Kurth F, Sander LE, Blüthgen N, Sawitzki B. 2022. Complement activation induces excessive T cell cytotoxicity in severe COVID-19. *Cell* **185**:493-512.e25. doi:10.1016/j.cell.2021.12.040

Griesenauer B, Paczesny S. 2017. The ST2/IL-33 axis in immune cells during inflammatory diseases. *Front Immunol* **8**:1–17. doi:10.3389/fimmu.2017.00475

Hata K, Yanagihara T, Matsubara K, Kunimura K, Suzuki K, Tsubouchi K, Eto D, Ando H, Uehara M, Ikegame S, Baba Y, Fukui Y, Okamoto I. 2023. Mass cytometry identifies characteristic immune cell subsets in bronchoalveolar lavage fluid from interstitial lung diseases. *Front Immunol* **14**:1145814. doi:10.3389/fimmu.2023.1145814

Ishikawa N, Hattori N, Yokoyama A, Kohno N. 2012. Utility of KL-6/MUC1 in the clinical management of interstitial lung diseases. *Respir Investig* **50**:3–13. doi:10.1016/j.resinv.2012.02.001

Kim ST, Sheshadri A, Shannon V, Kontoyiannis DP, Kantarjian H, Garcia-Manero G, Ravandi F, Im JS, Boddu P, Bashoura L, Balachandran DD, Evans SE, Faiz S, Ruiz Vazquez W, Divenko M, Mathur R, Tippen SP, Gumbs C, Neelapu SS, Naing A, Wang L, Diab A, Futreal A, Nurieva R, Daver N. 2021. Distinct Immunophenotypes of T Cells in Bronchoalveolar Lavage Fluid From Leukemia Patients With Immune Checkpoint Inhibitors-Related Pulmonary Complications. *Front Immunol* **11**:1–11. doi:10.3389/fimmu.2020.590494

Liao M, Liu Y, Yuan J, Wen Y, Xu G, Zhao J, Cheng L, Li J, Wang X, Wang F, Liu L, Amit I, Zhang S, Zhang Z. 2020. Single-cell landscape of bronchoalveolar immune cells in patients with COVID-19. *Nat Med* **26**:842–844. doi:10.1038/s41591-020-0901-9

Matsubara K, Kunimura K, Yamane N, Aihara R, Sakurai T, Sakata D, Uruno T, Fukui Y. 2021. DOCK8 deficiency causes a skewing to type 2 immunity in the gut with expansion of group 2 innate lymphoid cells. *Biochem Biophys Res Commun* **559**:135–140. doi:10.1016/j.bbrc.2021.04.094

Morelli T, Fujita K, Redelman-Sidi G, Elkington PT. 2022. Infections due to dysregulated immunity: an emerging complication of cancer immunotherapy. *Thorax* **77**:304–311. doi:10.1136/thoraxjnl-2021-217260

Owczarczyk K, Cascino MD, Holweg C, Tew GW, Ortmann W, Behrens T, Schindler T, Langford CA, St Clair EW, Merkel PA, Spiera R, Seo P, Kallenberg CGM, Specks U, Lim N, Stone J, Brunetta P, Prunotto M, RAVE-ITN Research Group. 2020. Fc receptor-like 5 and anti-CD20 treatment response in granulomatosis with polyangiitis and microscopic polyangiitis. *JCI insight* **5**:e136180. doi:10.1172/jci.insight.136180

Owczarczyk K, Lal P, Abbas AR, Wolslegel K, Holweg CTJ, Dummer W, Kelman A, Brunetta P, Lewin-Koh N, Sorani M, Leong D, Fielder P, Yocum D, Ho C, Ortmann W, Townsend MJ, Behrens TW. 2011. A plasmablast biomarker for nonresponse to

antibody therapy to CD20 in rheumatoid arthritis. *Sci Transl Med* **3**:1–10. doi:10.1126/scitranslmed.3002432

Postow MA, Sidlow R, Hellmann MD. 2018. Immune-Related Adverse Events Associated with Immune Checkpoint Blockade. *N Engl J Med* **378**:158–168. doi:10.1056/NEJMra1703481

Ravetch J V, Bolland S. 2001. IgG Fc Receptors. *Annu Rev Immunol* **19**:275–290. doi:10.1146/annurev.immunol.19.1.275

Rostamzadeh D, Kazemi T, Amirghofran Z, Shabani M. 2018. Update on Fc receptor-like (FCRL) family: new immunoregulatory players in health and diseases. *Expert Opin Ther Targets* **22**:487–502. doi:10.1080/14728222.2018.1472768

Sandor M, Lynch RG. 1993. Lymphocyte Fc receptors: the special case of T cells. *Immunol Today* **14**:227–231. doi:10.1016/0167-5699(93)90168-K

Skeoch S, Weatherley N, Swift A, Oldroyd A, Johns C, Hayton C, Giollo A, Wild J, Waterton J, Buch M, Linton K, Bruce I, Leonard C, Bianchi S, Chaudhuri N. 2018. Drug-Induced Interstitial Lung Disease: A Systematic Review. *J Clin Med* **7**:356. doi:10.3390/jcm7100356

Spitzer MH, Nolan GP. 2016. Mass Cytometry: Single Cells, Many Features. *Cell* **165**:780–91. doi:10.1016/j.cell.2016.04.019

Suzuki K, Yanagihara T, Matsumoto K, Kusaba H, Yamauchi T, Ikematsu Y, Tanaka K, Otsubo K, Inoue H, Yoneshima Y, Iwama E, Arimura-Omori M, Harada E, Hamada N, Okamoto I, Nakanishi Y. 2020. Immune-checkpoint profiles for T cells in bronchoalveolar lavage fluid of patients with immune-checkpoint inhibitor-related interstitial lung disease. *Int Immunol* **32**:547–557. doi:10.1093/intimm/dxaa022

Tanaka K, Yanagihara T, Ikematsu Y, Inoue H. 2018. Detection of identical T cell clones in peritumoral pleural effusion and pneumonitis lesions in a cancer patient during immune-checkpoint blockade. *Oncotarget* **9**:30587–30593. doi:10.18632/oncotarget.25743

Tasaka S, Hasegawa N, Kobayashi S, Yamada W, Nishimura T, Takeuchi T, Ishizaka A. 2007. Serum indicators for the diagnosis of pneumocystis pneumonia. *Chest* **131**:1173–1180. doi:10.1378/chest.06-1467

Thomas CF, Limper AH. 2004. Pneumocystis pneumonia. *N Engl J Med* **350**:2487–98. doi:10.1056/NEJMra032588

Van Raemdonck K, Van den Steen PE, Liekens S, Van Damme J, Struyf S. 2015. CXCR3 ligands in disease and therapy. *Cytokine Growth Factor Rev* **26**:311–327. doi:10.1016/j.cytogfr.2014.11.009

Vlaar APJ, de Bruin S, Busch M, Timmermans SAMEG, van Zeggeren IE, Koning R, ter Horst L, Bulle EB, van Baarle FEHP, van de Poll MCG, Kemper EM, van der Horst ICC, Schultz MJ, Horn J, Paulus F, Bos LD, Wiersinga WJ, Witzenrath M, Rueckinger S, Pilz K, Brouwer MC, Guo RF, Heunks L, van Paassen P, Riedemann NC, van de Beek D. 2020. Anti-C5a antibody IFX-1 (vilobelimab) treatment versus best supportive care for patients with severe COVID-19 (PANAMO): an exploratory, open-label, phase 2 randomised controlled trial. *Lancet Rheumatol* **2**:e764–e773. doi:10.1016/S2665-9913(20)30341-6

Yanagihara T, Tanaka K, Matsumoto K. 2020. A measuring method for occupancy of immune checkpoint inhibitors in the cell surface. *Biochem Biophys Res Commun* **527**:213–217. doi:10.1016/j.bbrc.2020.04.122

Yanagihara T, Tanaka K, Ota K, Kashiwagi E, Takeuchi A, Tatsugami K, Eto M, Nakanishi Y, Okamoto I. 2017. Tumor-infiltrating lymphocyte-mediated pleuritis followed by marked shrinkage of metastatic kidney cancer of the chest wall during nivolumab treatment. *Ann Oncol* **28**:2038–2039. doi:10.1093/annonc/mdx214

Supplemental Table 1. Mass cytometry antibody panels.

For CD45 barcoding

Label	Target	product_id	clone	Amount (uL)
89Y	CD45	3089003B	HI30	1
106Cd	CD45	3106001C	HI30	1
110Cd	CD45	3110001C	HI30	1
112Cd	CD45	3112001C	HI30	1
116Cd	CD45	3116001C	HI30	1
196Pt	CD45	3196001C	HI30	1

For antibody cocktail #1 (T cell panel)

Label	**Target**	**Product ID**	**Clone**	**Amount (uL)**
141Pr	CD3	3141019B	UCHT1	1
142Nd	CD11a	3142006B	HI111	0.5
143Nd	CD5	3143007B	UCHT2	1
145Nd	CD4	3145001B	RPA-T4	1
146Nd	CD8a	3146001B	RPA-T8	1
147Sm	CD7	3147006B	CD7-6B7	1
148Nd	CD274 (PD-L1)	3148017B	29E.2A3	1
149Sm	CD25 (IL-2R)	3149010B	2A3	1
150Nd	CD134 (OX40)	3150023B	ACT35	1
151Eu	CD2	3151003B	TS1/8	1
152Sm	CD95/Fas	3152017B	DX2	1
153Eu	TIM-3	3153008B	F38-2E2	1
154Sm	TIGIT	3154016B	MBSA43	1
155Gd	CD279 (PD-1)	3155009B	EH12.2H7	1
156Gd	CD183 (CXCR3)	3156004B	G025H7	1
158Gd	ST2 (R&D AF523)	Labeling (201158A)		1
159Tb	CD197 (CCR7)	3159003A	G043H7	1
160Gd	CD28	3160003B	CD28.2	1
161Dy	CD152 (CTLA-4)	3161004B	14D3	1
162Dy	CD69	3162001B	FN50	1
163Dy	CD272 (BTLA)	3163009B	MIH26	1
164Dy	CD45RO	3164007B	UCHL1	1

165Ho	CD223/LAG-3	3165037B	11C3C65	1
166Er	CD44	3166001B	BJ18	1
167Er	CD27	3167002B	O323	1
168Er	CD278/ICOS	3168024B	C398.4A	1
169Tm	CD19	3169011B	HIB19	1
170Er	CD45RA	3170010B	HI100	1
171Yb	CD226	3171013C	DX11	1
172Yb	CD273 (PD-L2)	3172014B	24F.10C12	1
173Yb	HLA-DR	3173005B	L243	0.5
174Yb	CD49d	3174018B	9F10	1
175Lu	CD14	3175015B	M5E2	2
176Yb	CD57	3176019B	HCD57	1
209Bi	CD16	3209002B	3G8	1

For antibody cocktail #2 (B cell/ myeloid cell panel)

Label	**Target**	**Product ID**	**Clone**	**Amount (uL)**
141Pr	CD3	3141019B	UCHT1	1
142Nd	CD19	3142001B	HIB19	0.5
143Nd	CD11b (Biolegend #301302)	Labeling(201143A)	ICRF44	0.5
144Nd	CD38	3144014B	HIT2	1
145Nd	CD163	3145010B	GHI/61	1
146Nd	CD64	3146006B	10.1	1
147Sm	CD11c	3147008B	Bu15	0.5
148Nd	IgA	3148007B	Polyclonal	1
149Sm	IgG (Biolegend #410701)	Labeling(201149A)		1
150Nd	CD138	3150012B	DL-101	0.5
151Eu	CD209 (Biolegend #343002)	Labeling(201209A)		1
152Sm	CD21	3152010B	BL13	1
153Eu	CD192 (CCR2)	3153023B	K036C2	1
154Sm	CD84	3154013B	CD84.1.21	1
156Gd	CD86	3156008B	IT2.2	1
158Gd	ST2 (R&D AF523)	Labeling (201158A)		1
159Tb	CD36 (Biolegend #336215)	Labeling(201159A)	5-271	1
160Gd	CD28	3160003B	CD28.2	0.5

164Dy	CD185/CXCR5	3164029B	RF8B2	1
165Ho	CD223/LAG-3	3165037B	11C3C65	1
166Er	CD24	3166007B	ML5	1
167Er	CD27	3167002B	O323	1
168Er	CD206 (MMR)	3168008B	44607	1
169Tm	CD32	3169020B	FUN-2	1
170Er	TIM-1 (Biolegend #353902)	Labeling(201170A)		1
171Yb	CD195 (CCR5)	3171017A	NP-6G4	1
172Yb	IgM	3172004B	MHM-88	1
173Yb	HLA-DR	3173005B	L243	0.5
174Yb	IgD (Biolegend #348235)	Labeling(201174A)	IA6-2	1
175Lu	CD14	3175015B	M5E2	2
176Yb	antiAPC-176Yb	3176007B	APC003	1
209Bi	CD16	3209002B	3G8	1

Supplementary Figure 1. A T cell gate ($CD2^{+}CD3^{+}$) and Citrus analysis of T cell populations in BALF cells from PCP, DI-ILD, and ICI-ILD.

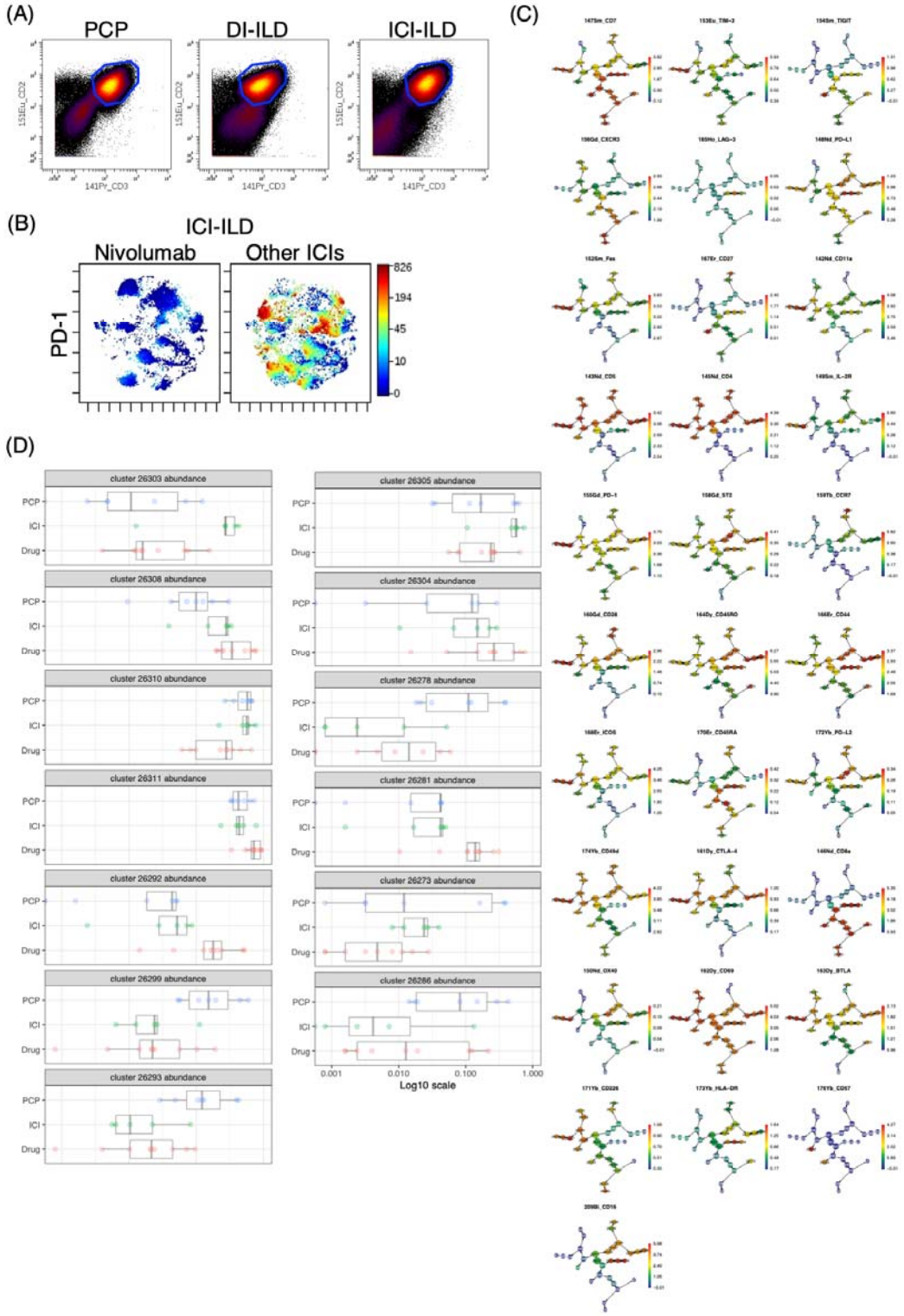

Supplementary Figure 2. The Citrus analysis of myeloid cell populations in BALF cells from PCP, DI-ILD, and ICI-ILD.

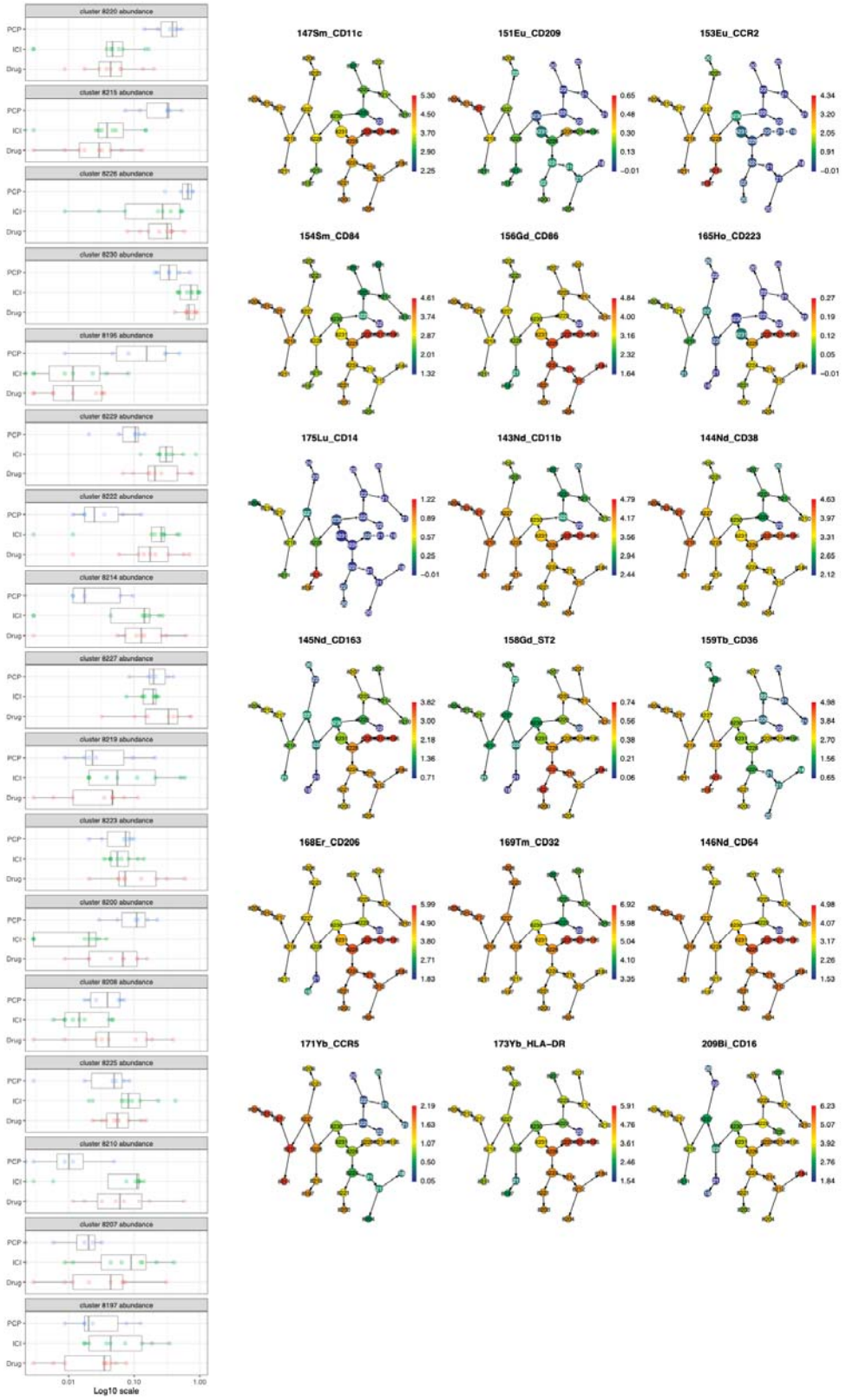

Supplementary Figure 3. The correlation matrix with the CTCAE and intensity of each T cell markers in PCP cases.

The correlation was calculated using the Pearson correlation coefficient. This involved correlating the CTCAE grade directly with the mean expression levels of each marker. The computations were conducted using GraphPad Prism version 9. CCR7, CD7, and CD57 are correlated with the severity (CTCAE) of PCP (p-values: 0.009, 0.035, and 0.039, respectively).

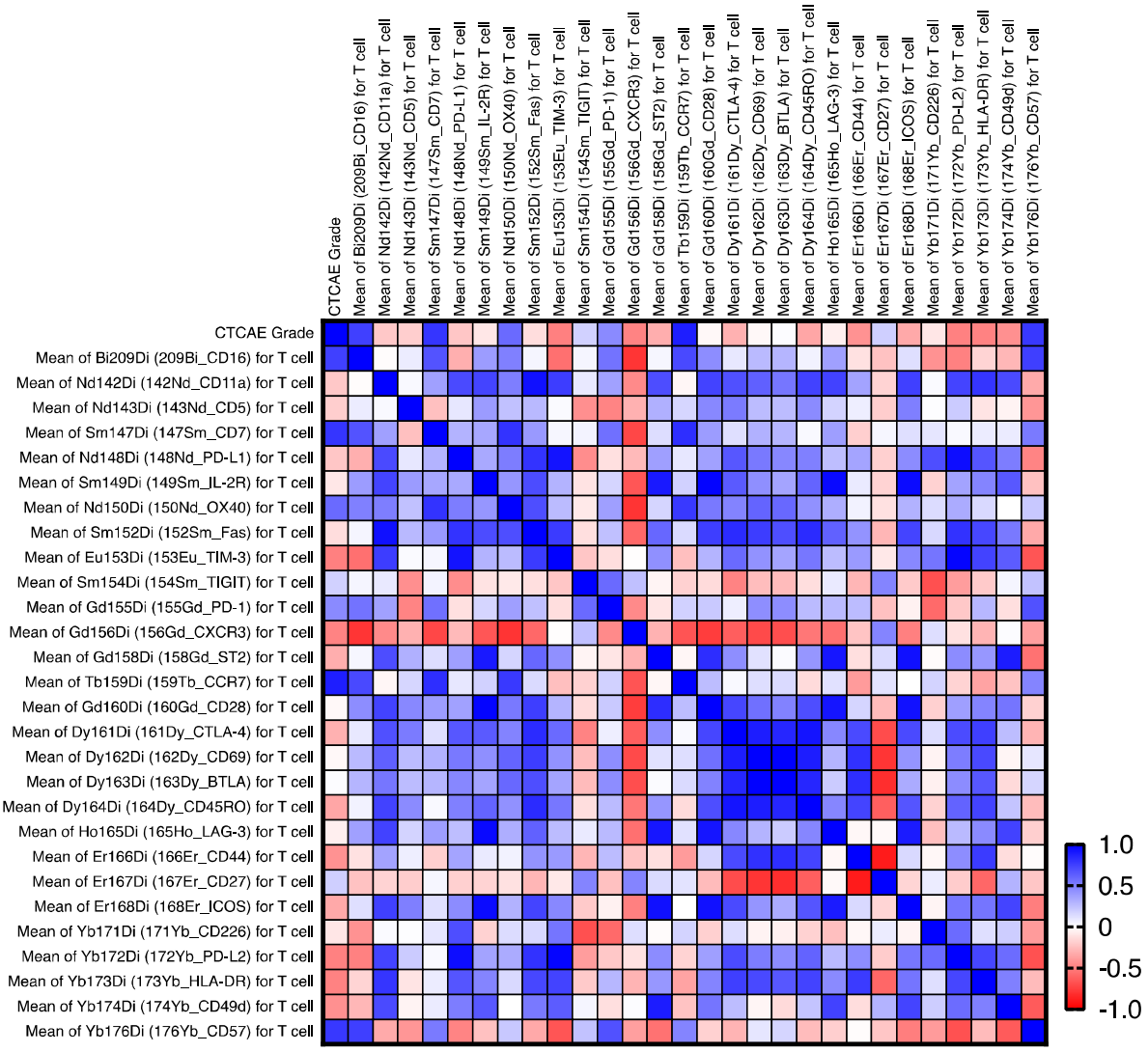

Supplementary Figure 4. T-cell marker expression on the UMAP projection in Figure 3B.

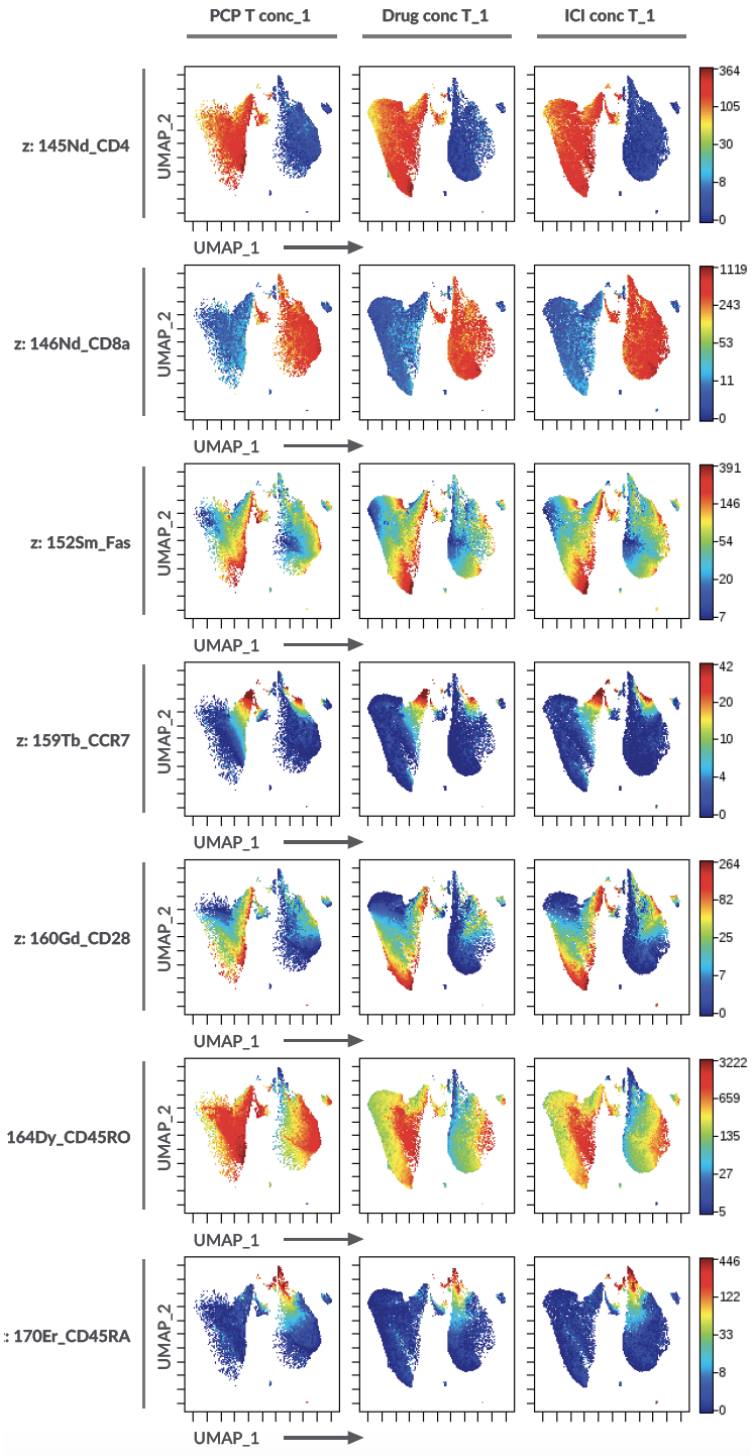

Supplementary Figure 5. Myeloid-cell marker expression on the UMAP projection in Figure 4A.

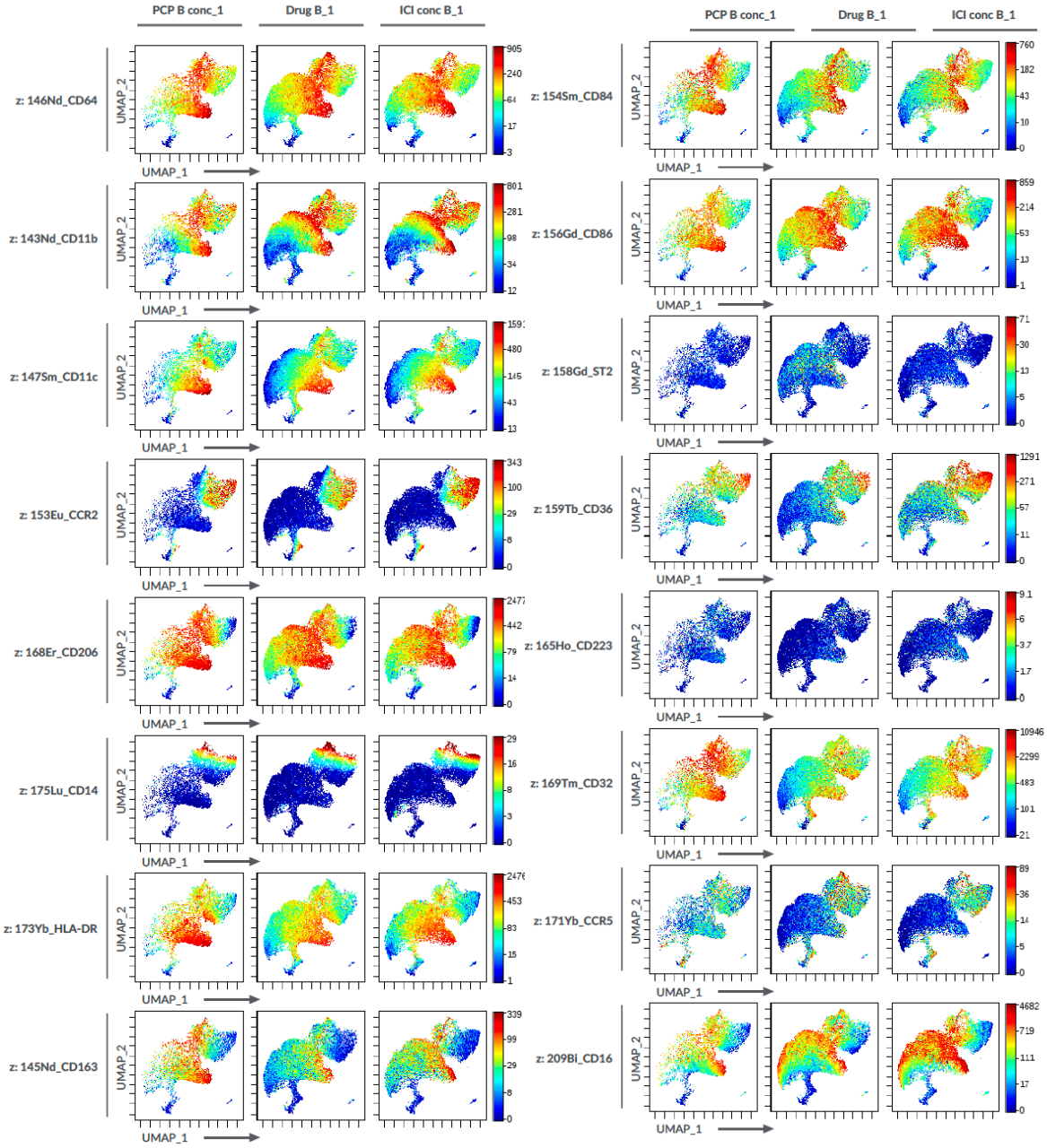
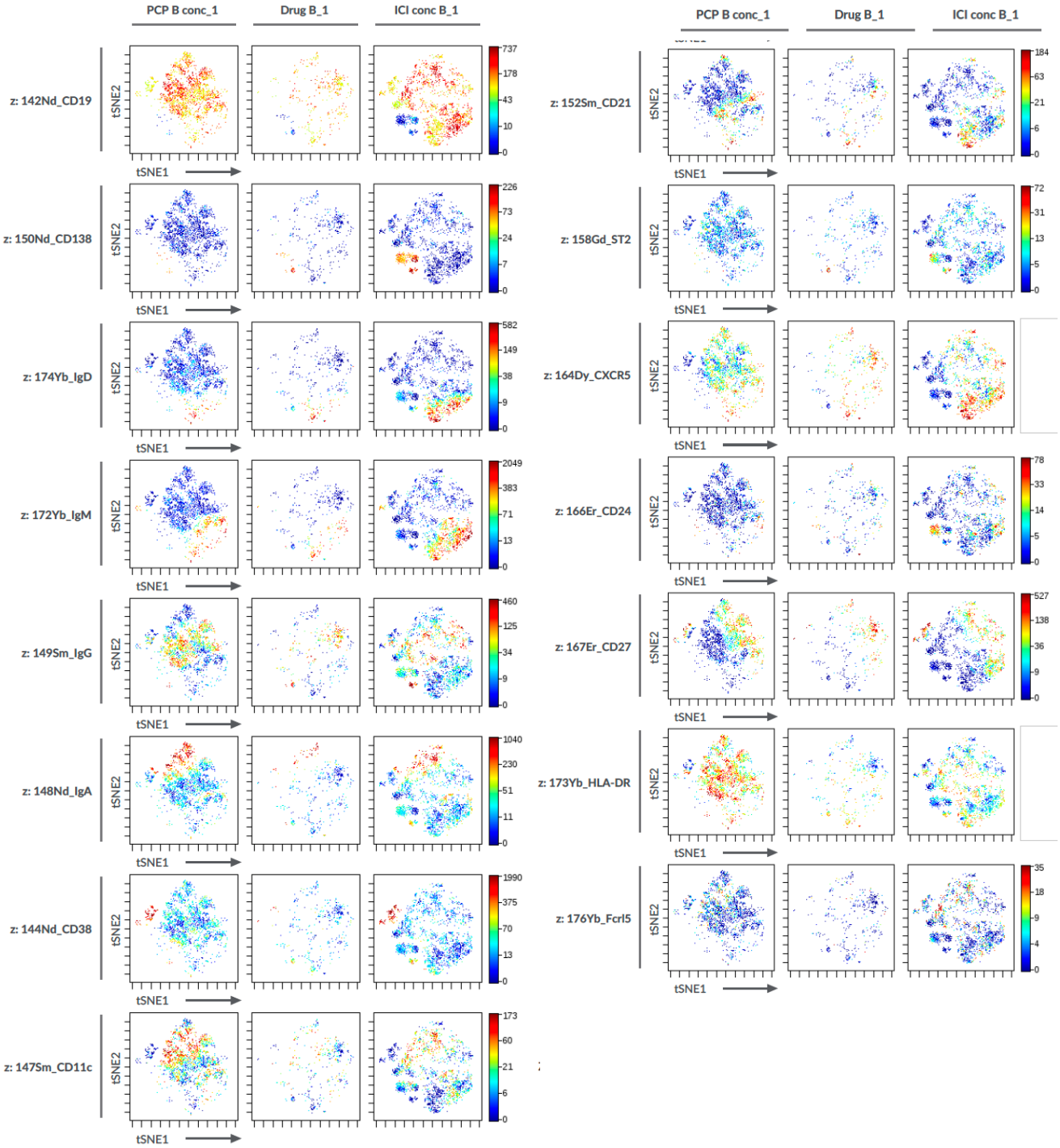
Supplementary Figure 6. B-cell marker expression on the tSNE projection in Figure 5B.